**Supporting Information**

# Organic DAST Single Crystal Meta-cavity Resonances at Terahertz Frequencies

Kai Fan,[†] Xiangdong Xu,[*,†] Yu Gu,[†] Zelin Dai,[†] Xiaomeng Cheng,[†] Jun Zhou, [‡] Yadong Jiang,[†] Ting Fan,[§] Jimmy Xu[‖]

[†]*State Key Laboratory of Electronic Thin Films and Integrated Devices, School of Optoelectronic Science and Engineering, University of Electronic Science and Technology of China (UESTC), Chengdu 610054, P.R. China*

[‡]*2011 Coordination Innovation Center for Terahertz, University of Electronic Science and Technology of China (UESTC), Chengdu 610054, P.R. China*

[§]*Chengdu Institute of Organic Chemistry, Chinese Academy of Sciences, Chengdu 610014, P.R. China*

[‖]*School of Engineering, Brown University, Providence, Rhode Island 02912, United States*

***Corresponding Author**

Tel: +86-28-83208959, Fax: +86-28-83206123, Email: xdxu@uestc.edu.cn (X.D. Xu)

## 1. Fabrication of Organic DAST Single Crystal Meta-cavity:

Our experiments indicated that it is difficult to fabricate the DAST single crystal cavity directly by the common microfabrication process, largely due to the undesired effects of the conventional lithographic process on an organic crystal. DAST single crystals will be dissolved in the common photoresist solvents, and will be etched or destroyed by the ultrasonic process. In order to tackle these problems, a shadow mask patterning technique was utilized. As displayed in Figure S1, our fabrication process is outlined briefly into two steps: fabrication of a $SiN_x$ film-based shadow mask (Figure S1a-f), and deposition of the metal antenna array on the DAST single crystal using the resulting $SiN_x$ film-based shadow mask (Figure S1g-h).

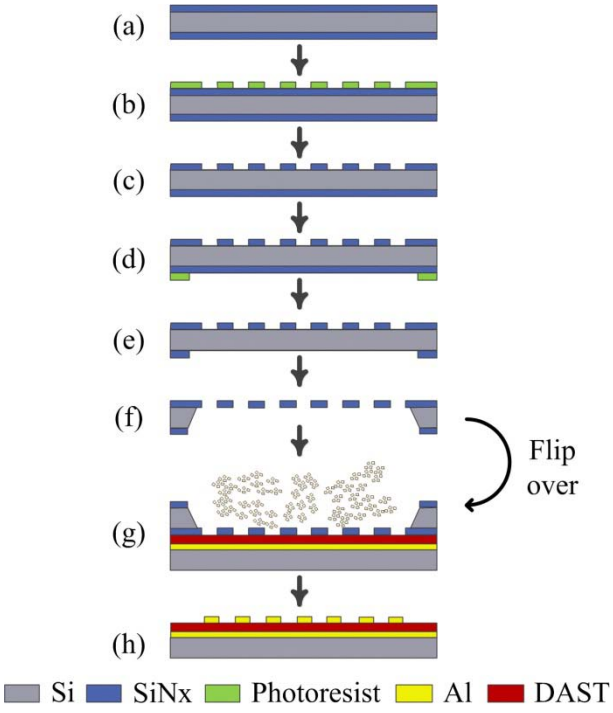


**Figure S1.** Schematic diagram showing the process for the fabrication of the DAST single crystal meta-cavity in this work.

Some of the $SiN_x$ film-based shadow masks with engraved pattern structures which had been successfully fabricated through the multi-step manufacturing process

in Figure S1 are displayed in Figure S2. A $SiN_x$ film-based shadow mask was handled carefully to be attached closely on the top surface of a DAST single crystal which had been pre-inductively-grown on a 200-nm-thick ground Al metal by a modified shear method.[S1] Subsequently, another metal (Al) layer with a thickness of 200 nm was deposited by electron beam evaporation, through which the square Al patch-antenna array was fabricated on the top surface of the DAST single crystal by the shadow mask metal patterning technique.[S2] Accordingly, the designed DAST single crystal meta-cavity was successfully fabricated, as displayed in Figure S3a.

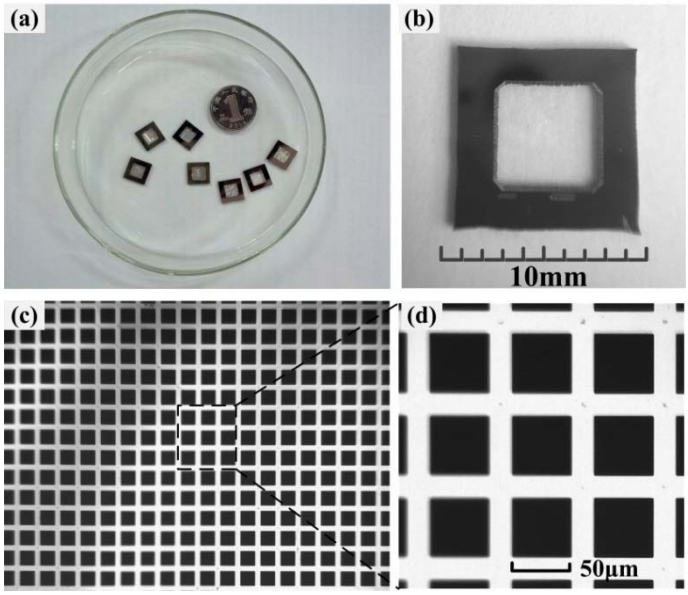


**Figure S2.** The fabricated $SiN_x$ film-based shadow masks used in this work.

## 2. Simulations

In the numerical simulations, the patch-antenna array DAST crystal cavity was simulated by a finite difference time domain software of CST Microwave Studio. First, in our simulations, the measured constant permittivities, i.e. $\varepsilon_a = 5.48 + i0.4$ and $\varepsilon_b = 2.81 + i0.2$ of DAST crystal along the **a**-axis and **b**-axis,[S3] were used as the constant permittivities for the dielectric layers in the 'uncoupled' cavities, respectively.

These simulation results reveal the resonance absorption peaks of a 'quasi-cavity' for the incident light polarized along the **a**- and **b**-axis, respectively. Second, the coupled DAST-cavity system was further simulated by using a frequency-dependent permittivity of DAST crystal, which can be described by a collection of Lorentz oscillators:[S3]

$$\tilde{\varepsilon}(\omega) = \varepsilon_{\infty} + \sum_j \frac{\eta_j \omega_j^2}{(\omega_j^2 - \omega^2) - 2i\gamma_j \omega} \quad \text{(S-1)}$$

where $\varepsilon_{\infty}$ is the high frequency dielectric constant, $\omega_j$ is the resonance frequency, $\eta_j$ denotes the oscillator strength, and $\gamma_j$ is the decay rate, respectively. The simulated DAST-cavity structure is illustrated in Figure S3b. The size of the ground Al metal is 2×2 $mm^2$, similar with the incident light spot size in the measurements. The conductivity of the Al metal is $1.0\times10^7$ S/m. Moreover, the square metal array is orientated to the DAST crystal edge with an angle of $55^o$ in the model.

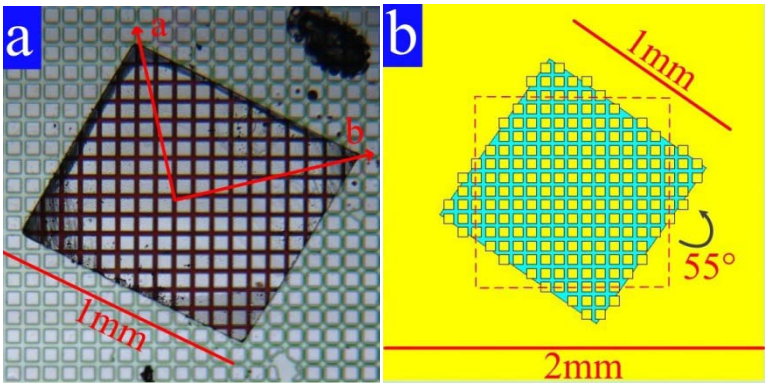


**Figure S3.** (a) The fabricated DAST single crystal patch-antenna array meta-cavity, and (b) schematic of the simulation model.

The parameters used in the simulations along the **a**- and **b**- axes of DAST crystal are displayed in Table S1. Since only one strong absorption peak at 1.10 THz in the 0.4–2.4 THz range was measured from the DAST single crystal along the **a**-axis

(Figure 3a in the manuscript text), as reported in Ref. S3, similar results would be obtained if the parameters of the DAST crystal were adopted from Ref. S3 or our measurements. However, four distinct absorption peaks, located at 0.84, 1.10, 1.50, and 1.67 THz, respectively, were experimentally measured from the bare DAST single crystal along the **b**-axis (Figure 3a in the manuscript text). Although the peak at ~0.8 THz was actually detected along the **b**-axis of DAST crystal in Ref. S3, this peak was not previously listed as the characteristic peak for DAST crystal along the **b**-axis.[S3] In order to better reflect the measured spectral features, the parameters extracted from our measurement results of the bare DAST single crystal (Figure 3a in the text) were utilized in the simulations of the coupled cavities along the **b**-axis.

**Table S1.** The parameters adopted from Ref. S3 and our measurements for the simulations.

| | $\omega_j$ | $\eta_j$ | $\gamma_j$ |
|---|---|---|---|
| **a**-axis | 1.10 | 0.79 | 0.39 |
| **b**-axis | 0.84 | 0.10 | 0.30 |
| | 1.10 | 0.27 | 0.31 |
| | 1.50 | 0.43 | 0.84 |
| | 1.67 | 0.10 | 0.20 |

Note: $\omega_j$, $\eta_j$, and $\gamma_j$ are the resonance frequency, oscillator strength, and decay rate, respectively.

Moreover, the curves of the refractive index along the **a**- and **b**- axes of DAST

crystal as a function of frequency that were plotted according to the data reported in Ref. S3 are shown in Figure S4, revealing the birefringence of DAST single crystal.

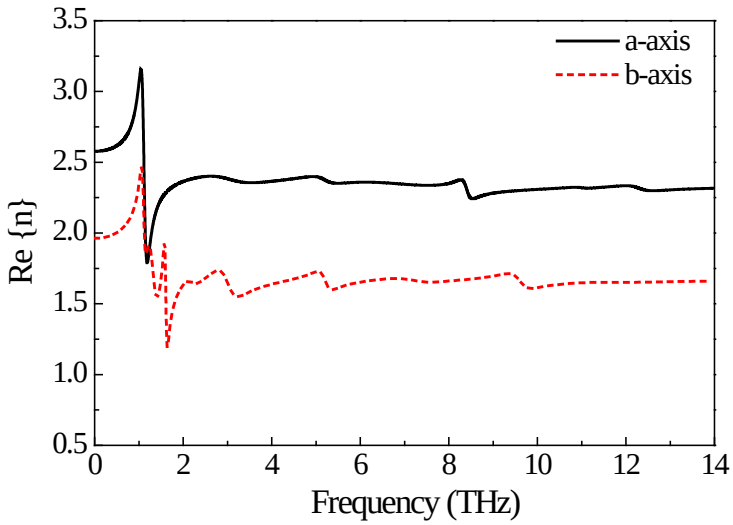


**Figure S4.** Refractive indices along the **a**- and **b**- axes of DAST single crystal plotted according to the data provided in Ref. S3.

With a fixed incident polarization angle along the **a**-axis, the simulation results of the 'uncoupled' and coupled patch-antenna array cavities simulated under various thicknesses *d* of the dielectric layer are shown in Figure 4 in the manuscript text. As comparison, the results simulated as a function of the square width W along the **a**-axis of DAST crystal are displayed in Figure S5. In this work, the 'uncoupled' and coupled cavities are referred to the antenna array cavities simulated without and with coupling to the dielectric materials. One can see that in the case of $d$=8 μm and W=52 μm (Figure 4b in the manuscript text) or $d$=27 μm and W=36 μm (Figure S5b), the cavity mode and the DAST optical phonon along the **a**-axis would similarly be on-resonance. Remarkably, both Figure S5b and Figure 4b in the manuscript text indicate that a Rabi splitting frequency of up to $2\Omega_R/2\pi$=0.37 THz, corresponding to 34% of the phonon resonance frequency of DAST at 1.10 THz, could be similarly achieved along the **a**-axis of DAST single crystal. Such Rabi splitting (34%) at

room temperature would be much larger than that (25%) along the **b**-axis of DAST crystal (see Figures 3c and 5b in the text) and those (22% of the respective resonance frequencies in the THz range)[S4,S5] previously observed at cryogenic temperatures in the typical complex inorganic quantum well microcavities. If a similar $SiN_x$ film-based shadow mask like that (Figure S2) in this work were used, a DAST single crystal with a size of 1×1 $mm^2$ and a much thinner thickness of 8 μm would be required for strong coupling Rabi splitting, as shown in Figure 4b in the manuscript text. Alternatively, if a DAST single crystal with a similar thickness of 27 μm as this work were used, a new $SiN_x$ film-based shadow mask with a much smaller width of 36 μm would be required for strong coupling Rabi splitting (Figure S5b). These suggest that a DAST single crystal with a size of 1×1 $mm^2$ and a thin thickness of 8 μm at W=52 μm or a new square metal patch with a small width W of 36 μm at *d*=27 μm would be required for such strong coupling.

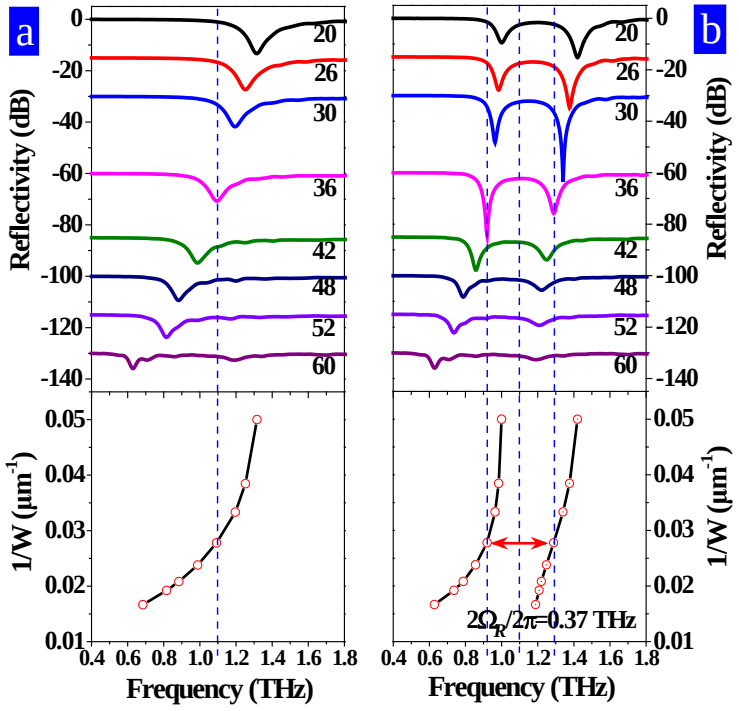


**Figure S5.** (a) Top: Simulated reflectivity spectra of the 'uncoupled' patch-antenna array cavities, which were simulated under the conditions of: the dielectric layer had a

thickness of 27 μm and a constant permittivity ($\varepsilon_a = 5.48 + i0.4$)[S3] of DAST crystal along the **a**-axis, while the square metal width W was ranged from 20 to 60 μm. Bottom: The positions of the reflectivity minima plotted in inverse widths 1/W. (b) Top: Simulated reflectivity spectra of the coupled cavities, which were simulated under the conditions of: the dielectric layer had a thickness of 27 μm and a frequency-dependent permittivity like that of DAST crystal as described in Equation (S-1), while the square metal width W was ranged from 20 to 60 μm. Strong coupling would be observed at a width W of 36 μm for the square metal patch in this case. Bottom: The black solid lines show the trends for the changes in the positions of the reflectivity dips. The response frequencies of the coupled system along the **a**-axis are split into two branches with a Rabi splitting of $2\Omega_R/2\pi$=0.37 THz.

For the simulations along the **b**-axis, we first simulated the coupling between the optical phonon mode of DAST crystal at 1.10 THz alone and the cavity mode. In this case, the THz spectra were simulated under the conditions of: the dielectric layer had a frequency-dependent permittivity like that of DAST crystal as described in Equation (S-1), and particularly, just one optical phonon mode of DAST at 1.10 THz was included in the simulations. Consequently, the contributions of the other three vibrational modes at 0.84, 1.50, and 1.67 THz for DAST crystal along the **b**-axis to the coupling are eliminated. Figure S6b reveals that if the thickness *d* of the dielectric layer is 27 μm, as that for the DAST single crystal in the fabricated meta-cavity, both the two overlapped peaks at 1.10 THz for the uncoupled material and cavity modes disappears, and instead, two new reflectivity minima at 0.94 and 1.22 THz appear, where one (0.94 THz) is red-shifted while another (1.22 THz) is blue-shifted, relative to the 1.10 THz peak. For comparison, the transmission spectra

for DAST crystal along the **b**-axis were further simulated in two ways. In the first case, all the parameters were adopted from Ref. S3, where the peak at 0.84 THz was not included. In this way, we just investigated the effects of *d* on the spectra along the **b**-axis (Figure S6c). In the second case, the spectra along **b**-axis under different *d* were similarly simulated, but differently, the parameters were extracted from our measurements (Figure 3a in the manuscript text), where the weak peak at 0.84 THz was included in the simulations (Figure S6d). As shown in Figures S6c and S6d, similar Rabi splitting values of 0.28 THz can be extracted from these two cases, both agreeing well with the experimental measurements (Figure 3c in the manuscript text). This suggests that the Rabi splitting energy (0.28 THz) experimentally measured is credible. It is worth noting that compared with the first case, better accordance of the spectral features simulated in the second case with those experimentally measured (Figure 3c in the manuscript text) is seen in Figure S6d. Further inspection reveals that the peak positions and amplitudes at $d$=27 μm are different in Figure S6b and S6d. This is attributed to that only one vibrational mode of DAST at 1.10 THz was considered in Figure S6b, whereas four vibrational modes at 0.84, 1.10, 1.50, and 1.67 THz for DAST crystal along the **b**-axis were simultaneously included in the simulations shown in Figure S6d. The contributions from the other three vibrational modes, especially from the two strong ones at 1.50 and 1.67 THz as shown in Figure 3a, to the coupling at 1.10 THz lead to the observation of different amplitudes and red-shifts of the coupled peaks (Figure S6d). Despite of these differences, the response frequencies of the coupled system simulated with only one vibrational mode of DAST crystal at 1.10 THz are split into two branches with a Rabi splitting of $2\Omega_R/2\pi$=0.28 THz (Figure S6b), similar to that ($2\Omega_R/2\pi$=0.28 THz) experimentally measured (Figure 3c in the text) and numerically simulated (Figure S6d) with four

vibrational modes of DAST crystal. This suggests that the contributions from the other three vibrational modes at 0.84, 1.50, and 1.67 THz of DAST crystal along the **b**-axis mainly affect the amplitudes of the coupled modes, but not as much the splitting energy. This also verifies that the Rabi splitting of $2\Omega_R/2\pi$=0.28 THz in Figure 3c can rise from the coupling between the optical phonon mode of DAST at 1.10 THz and the meta-cavity mode.

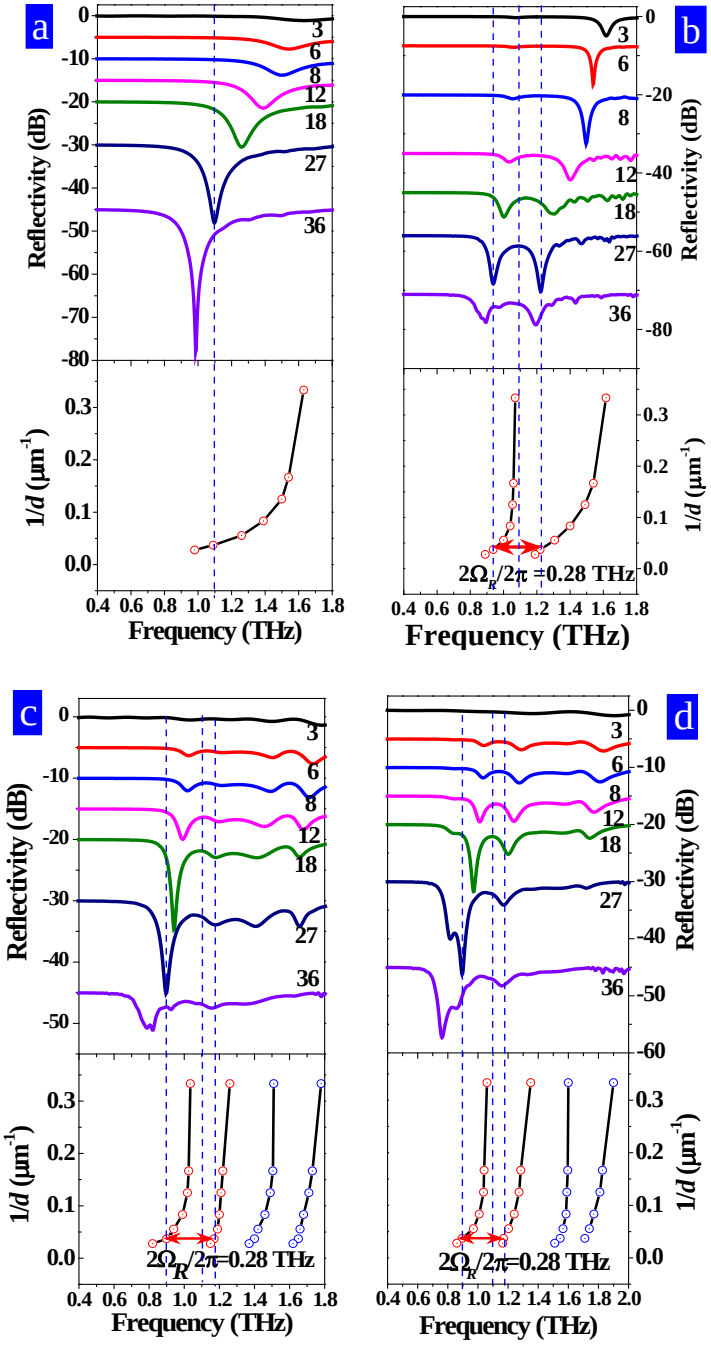

**Figure S6.** (a) Top: Simulated reflectivity spectra of the 'uncoupled' patch-antenna array cavities with various thicknesses *d* (3–36 μm) for the dielectric layer, where the dielectric layer had a constant permittivity ($\varepsilon_b = 2.81 + i0.2$) of DAST crystal along the **b**-axis. Bottom: The frequency positions of the reflectivity minima plotted in inverse thicknesses (1/*d*). The black solid line shows the trend for the change in the position of the reflectivity dip. (b) Top: Simulated reflectivity spectra of the coupled cavities with various thicknesses *d* (3–36 μm) for the dielectric layer, where the dielectric layer had a frequency-dependent permittivity like that of DAST crystal as described in Equation (S-1), but just one absorption peak at 1.10 THz was included in the simulations. Rabi-split reflectivity is seen on strong coupling at a thickness *d*=27 μm for the dielectric layer. Bottom: The response frequencies of the coupled system are split into two branches with a Rabi splitting of $2\Omega_R/2\pi$=0.28 THz. (c) Top: Simulated reflectivity spectra of the coupled cavities with various thicknesses *d*, where the dielectric layer had a frequency-dependent permittivity like that of DAST crystal as described in Equation (S-1), and three absorption peaks at 1.10, 1.50, and 1.67 THz were included in the simulations. Rabi-split reflectivity is seen on strong coupling at a thickness *d*=27 μm for the DAST single crystal. Bottom: The response frequencies of the coupled system along the **b**-axis are split into two branches with a Rabi splitting of $2\Omega_R/2\pi$=0.28 THz. (d) Top: Simulated reflectivity spectra of the coupled cavities with various thicknesses *d*, where the dielectric layer had a frequency-dependent permittivity like that of DAST crystal as described in Equation (S-1), and four absorption peaks at 0.84, 1.10, 1.50, and 1.67 THz were included in the simulations. Rabi-split reflectivity is seen on strong coupling at a thickness *d*=27 μm for the DAST single crystal. Bottom: The response frequencies of the coupled system along the **b**-axis are split into two branches with a Rabi splitting of

$2\Omega_R/2\pi$=0.28 THz.

## References


(S1) Fan, K. Design and analysis of DAST-based metamaterials. *Master Degree Dissertation*, University of Electronic Science and Technology of China (UESTC), P.R. China, 2016.

(S2) Tao, H.; Chieffo, L. R.; Brenckle, M. A.; Siebert, S. M.; Liu, M.; Strikwerda, A. C.; Fan, K.; Kaplan, D. L.; Zhang, X.; Averitt R. D.; Omenetto F. G. Metamaterials on paper as a sensing platform. *Adv. Mater.* **2011**, *23*, 3197-3201.

(S3) Cunningham, P. D.; Hayden, L. M. Optical properties of DAST in the THz range. *Opt. Express* **2010**, *18*, 23620-23625.

(S4) Todorov, Y.; Andrews, A. M.; Sagnes, I.; Colombelli, R.; Klang, P.; Strasser, G.; Sirtori, C. Strong light-matter coupling in subwavelength metal-dielectric microcavities at terahertz frequencies. *Phys. Rev. Lett.* **2009**, *102*, 186402.

(S5) Dietze, D.; Andrews, A. M.; Klang, P.; Strasser, G.; Unterrainer, K.; Darmo, J. Ultrastrong coupling of intersubband plasmons and terahertz metamaterials. *Appl. Phys. Lett.* **2013**, *103*, 201106.